

Numerical simulation of bubble deformation and breakup under simple linear shear flows

Mitsuhiro Ohta^{a,b,*}, Tetsuya Ueta^b, Yozo Toei^c, Edwin Jimenez^d, Mark Sussman^e

^a*Department of Mechanical Science, Graduate School of Technology, Industrial and Social Sciences, Tokushima University, 2-1 Minamijyousanjima-cho, Tokushima 770-8506, Japan*

^b*Department of Mechanical Engineering, Graduate School of Technology, Industrial and Social Sciences, Tokushima University, 2-1 Minamijyousanjima-cho, Tokushima 770-8506, Japan*

^c*High Performance Plastics Company, Sekisui Chemical Co., Ltd., 2-1 Hyakuyama, Mishimagun Shimamoto-cho, Osaka 618-0021, Japan*

^d*Spectral Numerical, LLC, 1942 Broadway St., STE 314C, Boulder, CO 80302, USA*

^e*Department of Mathematics, Florida State University, Tallahassee, FL 32306, USA*

Abstract

Numerical simulations are presented for the deformation and breakup of a bubble in liquids undergoing simple linear shear flow. Numerical results are obtained using a projection method for incompressible two-phase flow. The method represents interfaces using the sharp interface coupled level set and Volume-Of-Fluid (CLSVOF) method. To verify our numerical algorithm and provide a basis for comparison, we also present simulation results that compare with previous, more popular, drop deformation and rupture simulations. The numerical results reveal that the shear-induced bubble deformation and breakup process differs significantly from that of the analogous drop system under similar flow conditions. The first distinguishing factor for bubble breakup is that the magnitude of shear flow necessary for causing rupture is much larger than that in the drop system case. In other words, a larger Reynolds number is needed to induce bubble breakup. The second distinct feature of the bubble system versus the drop system is that the bubble does not maintain a stable deformed shape as the system parameters approach the critical “breakup” Reynolds number. It is asserted that the differences in morphology for a bubble undergoing breakup versus a drop in the same process can be attributed to the density and viscosity ratio of the corresponding two-phase flow systems. The critical conditions for bubble breakup with respect to the Reynolds and capillary numbers are determined for several cases.

Keywords: Bubble deformation, bubble breakup, shear flow, CFD

*Corresponding author: m-ohta@tokushima-u.ac.jp

1 **1. Introduction**

2 Bubble dynamics in shear flow, including breakup, is critically important
3 for various gas-liquid scientific and engineering processes. We refer the reader
4 to the following experimental studies relating to bubble deformation in foaming
5 processes, microfluidic devices, microbubbles in the blood circulation system,
6 materials processing, pharmaceuticals, minerals engineering, bubble column re-
7 actor, and cosmetics[4, 25, 3, 8, 9, 50, 10, 53]. In particular, it is the study
8 of bubble deformation as it pertains to high-performance plastics applications
9 that motivate this work.

10 This article presents computational studies of shear-driven deformation and
11 breakup of a bubble in insoluble viscous liquids. Studying bubble break-up, in
12 which we focus only on the balance of the wall driving force and bubble surface
13 tension force, via computation rather than (terrestrial) experiments simplifies
14 the process of setting a combination of precise, simple shear flow conditions, low
15 Ca ($Ca = \mu_m U / \sigma$) conditions, low-density ratio, and low viscosity ratios. The
16 physical properties that distinguish bubble and drop studies are expressed in
17 terms of the density ratio $\lambda = \rho_b / \rho_m$ and the viscosity ratio $\eta = \mu_b / \mu_m$, where
18 ρ is the fluid density, μ is the viscosity and the subscripts “b” and “m” denote
19 the “bubble” or “drop” and the “matrix fluid”, respectively. For a bubble in
20 an insoluble, viscous liquid, $\lambda \simeq 0$ and $\eta \simeq 0$, whereas most (terrestrial) studies
21 dealing with a drop in an immiscible viscous liquid take $\lambda = 1$ and $\eta \simeq 1$.

22 In this work, we focus on identifying critical flow states numerically, in terms
23 of dimensionless quantities, that specify the extreme conditions at which a bub-
24 ble in shear flow first transitions from deformation to breakup. We validate our
25 numerical method by examining the sensitivity of the critical bubble deforma-
26 tion and break-up flow states with respect to the grid size. An advantage of
27 studying shear-driven bubble deformation and breakup computationally rather
28 than experimentally is that we can easily modify fluid physical properties and
29 external properties (e.g. we can easily modify the gravity force, in order to com-
30 pare with the analogous drop case or compare with microgravity conditions) in
31 order to isolate the sensitivity of deformation and breakup to physical parame-
32 ters. In our computations, the time-evolution of the boundary between gas and
33 liquid is tracked with a Coupled-Level-Set and Volume-Of-Fluid (CLSVOF) in-
34 terface capturing algorithm [42, 44]. The rationale for the CLSVOF method
35 is that the hybrid method represents the (complex) gas-liquid interfaces with
36 minimal volume loss (property of the Volume-Of-Fluid method) and minimal
37 error in the approximation of the surface tension force (property of the Level-Set
38 method).

39 We focus on determining critical physical conditions in which the breakup of
40 a bubble occurs in shear flow because it is important to identify the parameter
41 regimes in which a relatively simple system transitions from stable to unstable.
42 Specifically, we ascertain the critical Reynolds number (Re_c) corresponding to
43 the bubble breakup onset condition as a function of Ca .

44 In previous studies on the motion of bubble deformation in a simple shear
45 flow [37, 25], only findings for bubble deformation under very low Re number

46 conditions ($Re \ll 1$) have been reported. This is understandable since a low
47 Reynolds number matrix fluid mitigates the effect of gravity on distorting the
48 comparison with the drop case. In this work, we determine, for the first time,
49 the critical Reynolds number ($Re \gg 1$) that leads to bubble breakup. Additionally,
50 our computational studies reveal characteristics that distinguish a drop's
51 deformation and breakup processes versus those of a bubble.

52 We remark that there have been a number of articles on the study of lift
53 of slightly deformable bubbles[11, 23]. We reiterate, though, that for bubble
54 deformation and breakup in shear flows, only a few articles exist: [52, 51, 38].
55 These previous studies mainly examined the dynamics (e.g., rotation angle) of
56 bubble deformation in shear flow. Concerning bubble breakup, Wei et al. [52]
57 presented one numerical result for a bubble breakup process under the condition
58 of Ca (capillary number) = 35. Sharifi et al[38] presented two results for bubble
59 breakup corresponding to $Ca = 7.5$ and $Ca = 11.2$. We point out that all of the
60 previous computational research on bubble deformation (and breakup) under
61 shear driven flow[52, 51, 38] use the (explicit) Lattice Boltzmann method. For
62 accurately computing the tensile strength of a bubble, and accurately comput-
63 ing threshold parameters for break-up (what we do in this article, and what
64 was not done in previous work), it is critical that a numerical method directly
65 enforces the velocity continuity condition and the gas-liquid interface normal
66 jump conditions. We contend that a projection method (e.g. this paper and
67 [55, 56, 29]) is the more appropriate (albeit slower) method for our study rather
68 than the Lattice Boltzmann method. Also, in contrast to the Lattice Boltz-
69 mann method, our interface “capturing” method, the CLSVOF method[42, 44],
70 maintains the gas/liquid interface as sharp, enables accurate approximation of
71 the surface tension force, and by construction the CLSVOF method preserves
72 mass and volume within a fraction of a percent. The results that we present in
73 this article (see e.g. section 3.3.2) regarding measuring the tensile strength of
74 a bubble are unique and validated with respect to comparisons with previous
75 experimental data and grid refinement studies. Admittadly, each simulation on
76 the finest resolution takes over a half a year to complete on a workstation be-
77 cause of the following unavoidable factors: (i) the large density-ratio projection
78 method requires the solution of a large sparse, ill-conditioned, matrix system at
79 each time step, (ii) the finer the mesh, the more precise the measured threshold,
80 and right at the threshold (Taylor Deformation parameter $D \approx 1$), oscillatory
81 behaviour is observed delaying the determination of breakup or not. Finally,
82 the larger the deformation parameter D , the longer we must make our compu-
83 tational domain (bigger domain aspect ratio!) thereby adversely effecting the
84 condition number even more for carrying our the pressure projection.

85 To highlight the mechanisms of bubble deformation and breakup in a shear
86 flow, we juxtapose the bubble results with those of a drop (for terrestrial ex-
87 periments, when the density ratio of drop to matrix is very close to one!). We
88 remark that while the study of critical tensile strength parameters for the bub-
89 ble is sparse, there have been many studies for the simpler drop problem. For
90 completeness, we give a brief overview of previous “tensile strength” studies
91 pertaining to drops.

92 The study of the deformation and breakup of a drop in immiscible vis-
93 cous liquids undergoing simple linear shear flow has been investigated exten-
94 sively due to its fundamental importance to emulsion processes, materials pro-
95 cessing, mixing, and reaction devices. The pioneering experimental work on
96 this problem was performed by Taylor in the early 1930s [47, 48], and the
97 subsequent theoretical and experimental progress up to the 1980s and 1990s
98 was reviewed in [30] and [39], respectively. By the 2000s, progress in com-
99 putational fluid dynamics (CFD) techniques and increased access to powerful
100 computing resources led to a surge of research focused on direct simulations
101 of this problem. In particular, detailed computational investigations of drop
102 breakup, based on a Volume-of-Fluid (VOF) method [13] were presented in
103 [24, 34, 36, 35, 20, 31, 32, 33]. Since then, the literature on computational stu-
104 dies on the deformation and breakup of a single or several drops in shear flow
105 has continued to grow [6, 15, 54, 2, 17, 7, 21, 22, 16, 12, 1, 57] and a variety
106 of numerical techniques have been developed to tackle this problem, including
107 boundary-integral approaches [5, 18], lattice Boltzmann methods [14, 21], front
108 tracking schemes [49], and interface-capturing level set methods [43].

109 Thus, a lot of studies about the deformation and breakup of a drop in sim-
110 ple linear shear have been presented so far. In contrast, few studies have been
111 conducted on bubble deformation and breakup. We reiterate why there have
112 been few studies regarding the “tensile strength” of bubbles. Experimentally, if
113 one wants to isolate the interplay of shearing force with the bubble surface ten-
114 sion force, in the moderate to high Reynolds number regime, and low Capillary
115 number regime, one is restricted to microgravity conditions. Computational ex-
116 periments are difficult too. In order to accurately compute the tensile strength of
117 a bubble, one must resort to a combination of parallel computing, the multigrid
118 preconditioned conjugate gradient method[46, 44] for poorly conditioned large
119 sparse matrix systems, adaptive mesh refinement[58, 44], and a robust, volume
120 preserving interface tracking method (we use the CLSVOF method[42, 44]).

121 2. Problem Description

122 Figure 1(a) shows a schematic of the computational system for our studies
123 of a bubble (or drop) in shear flow. The computational domain consists of a
124 three-dimensional rectangular domain with the dimensions of L (length) $\times W$
125 (width) $\times H$ (height). The size of L , W and H was determined after considera-
126 tion of the sensitivity of numerical results to the domain size; numerical studies
127 of domain-size dependence are presented in Section 3.3. All computational re-
128 sults that follow were obtained from numerical solutions of the three-dimensional
129 governing equations for gas-liquid/liquid-liquid flows. Computations are initial-
130 ized with a spherical bubble (or drop) of radius $R = 5$ mm set at the center of
131 the computational domain. The bubble (or drop) is then subjected to a linear
132 shear flow generated by the motion of the top and bottom plates, which have
133 constant velocity $+V$ and $-V$, respectively. In the interior of the domain, the
134 initial velocity condition is assumed to be a simple linear profile and periodic

¹³⁵ boundary conditions are imposed along the x and y directions. Mathematically,
¹³⁶ the initial and boundary conditions are described as follows:

$$\begin{aligned}\phi(x, y, z, 0) &= \sqrt{(x - \frac{L}{2})^2 + (y - \frac{W}{2})^2 + (z - \frac{H}{2})^2 - R} \quad (1) \\ \mathbf{u}(x, y, z, 0) &= \begin{pmatrix} \frac{2V}{H}(z - \frac{H}{2}) \\ 0 \\ 0 \end{pmatrix} \\ \phi(x + L, y, z, t) &= \phi(x, y, z, t) \quad \phi(x, y + W, z, t) = \phi(x, y, z, t) \\ \mathbf{u}(x, y, H, t) &= \begin{pmatrix} V \\ 0 \\ 0 \end{pmatrix} \quad \mathbf{u}(x, y, 0, t) = \begin{pmatrix} -V \\ 0 \\ 0 \end{pmatrix} \\ \mathbf{u}(x + L, y, z, t) &= \mathbf{u}(x, y, z, t) \quad \mathbf{u}(x, y + W, z, t) = \mathbf{u}(x, y, z, t)\end{aligned}$$

¹³⁷ $\phi(x, y, z, t)$ is a material indicator function which is positive in the “matrix”
¹³⁸ fluid and negative in the bubble (or drop) fluid. $\mathbf{u}(x, y, z, t)$ is the velocity.

¹³⁹ Common dimensionless physical parameters used to describe gas-liquid or
¹⁴⁰ liquid-liquid two-phase flows include the Reynolds (Re), Weber (We) (or Ca (=
¹⁴¹ We/Re)) and Froude (Fr) numbers. Gas-Liquid and Liquid-Liquid two-phase
¹⁴² flow problems are also determined by the density ratio λ and the viscosity ratio
¹⁴³ η . In the present study, in order to clearly isolate the effects of λ and η , and
¹⁴⁴ isolate the balance of the driving wall force with the bubble surface tension
¹⁴⁵ force, the effect of gravity is not considered ($g = 0$) so that we ignore the effect
¹⁴⁶ of the Fr number ($= \frac{\Gamma R}{\sqrt{gR}}$).

¹⁴⁷ When comparing with previous drop studies, we fix $\lambda = 1$ for the drop cases.
¹⁴⁸ As a result, (for $\lambda = 1$) the following dimensionless physical parameters are used
¹⁴⁹ to describe the problem of drop deformation/breakup in shear flow:

$$Re = \frac{\rho_m U R}{\mu_m}, \quad Ca = \frac{\mu_m U}{\sigma}, \quad \eta = \frac{\mu_b}{\mu_m} \quad m = \text{matrix fluid} \quad (2)$$

¹⁵⁰ U is the velocity scale and σ denotes the surface tension. For the problem of
¹⁵¹ shear-induced drop deformation and breakup, the velocity is set to $U = \Gamma R$,
¹⁵² where the shear-rate is $\Gamma = 2V/H$. As mentioned in the introduction, most
¹⁵³ previous drop studies set $\eta = 1$ (e.g. Li et al. [24]). Thus, for comparison
¹⁵⁴ with previous drop deformation and breakup problems, we set $\lambda = \eta = 1$ (and
¹⁵⁵ also neglect the effect of gravity so that $g = 0$). On the other hand, in our
¹⁵⁶ computations for bubble deformation, we set the density and viscosity of air to
¹⁵⁷ be $\rho_b = 1.2 \text{ kg/m}^3$ and $\mu_b = 1.8 \times 10^{-5} \text{ Pa}\cdot\text{s}$ respectively. We emphasize that for
¹⁵⁸ consistency with previous studies (Li et al. [24], Rust and Manga [37], Müller-
¹⁵⁹ Fischer et al. [25], Komrakova et al. [21], Amani et al. [1]), we computationally
¹⁶⁰ examine the deformation and breakup of a bubble in simple linear shear flow
¹⁶¹ as a function of the Re and Ca numbers. That is to say, by setting $g = 0$,
¹⁶² we are isolating the effect of only varying Re and Ca on bubble deformation
¹⁶³ and breakup. In our controlled study, we determine the critical Re_c versus Ca

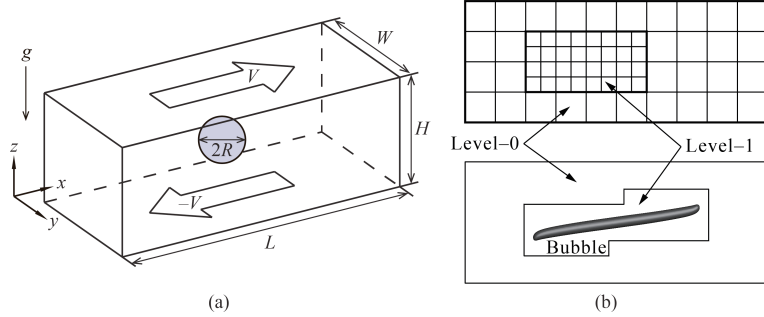


Figure 1: (a) Computational domain schematic for a bubble or drop in shear flow. Gravity is set to zero in our computations in order to isolate the effects of density and viscosity ratios. (b) (upper panel) a two-level adaptive mesh refinement (AMR) grid schematic corresponding to one of our simulations; (lower panel) snapshot of bubble deformation in simple linear shear flow.

164 curve in which Re_c corresponds to the threshold of bubble (or drop) breakup.
 165 We determine the critical Re_c versus Ca curve for strategic pairs of the density
 166 ratio and viscosity ratio.

167 In our computations, the density of the matrix fluid is fixed at $\rho_m = 1000$
 168 kg/m^3 . The surface tension at the bubble (drop) interface is $\sigma = 2.5 \times 10^{-2}$
 169 N/m . The values of Re and Ca in our simulations are controlled by changing
 170 the values of μ_m and V . Specifically, we set $\mu_m = 2.0 \times 10^{-2} \sim 6.0 \times 10^{-2}$
 171 $\text{Pa}\cdot\text{s}$ and $V = \text{about } 1.1 \sim 1.3 \text{ m/s}$. As a consequence, for studying bubble
 172 deformation and break-up, the density and viscosity ratios satisfy $\lambda = 1.2 \times 10^{-3}$
 173 and $\eta < 1.0 \times 10^{-3}$.

174 For readers' reference, we describe the effect of gravity here. When we apply
 175 $g = 9.8 \text{ m/s}^2$, Fr can be $Fr = 1.7 \sim 1.9$ in our computations. Although the
 176 values of Fr are not so large, the effect of gravity (bubble rise motion) may not
 177 be completely negligible in terms of Fr . However, bubbles in our computations
 178 reach the breakup by way of deformation very quickly at $t = \text{about } 0.5 \text{ s}$.
 179 Accordingly, it is expected that the effect of gravity (bubble rise motion) can
 180 be small for the behavior of bubble deformation and breakup around critical Re
 181 number conditions in our study.

182 3. Numerical Analysis

183 3.1. Numerical method and governing equations

184 Numerical results were obtained using the interface capturing Coupled Level
 185 Set and Volume of Fluid (CLSVOF) method (Sussman and Puckett [42], Suss-
 186 man et al. [44]), which is based on a fixed grid finite volume algorithm. The
 187 CLSVOF method is a robust numerical technique that combines some of the ad-
 188 vantages of the Volume of Fluid (VOF) method (Hirt and Nichols [13]) and the
 189 Level Set (LS) (Sussman et al. [43]) method while overcoming their weaknesses.
 190 In the VOF method, the Volume Fraction function, F , is used to represent

191 the interface. The values of F correspond to the volume fraction of liquid in
 192 a given computational cell. In other words, $F = 0$ when a computational cell
 193 contains only gas and $F = 1$ when a computational cell contains only liquid.
 194 If $0 < F < 1$, then a computational cell contains the gas-liquid interface. The
 195 VOF method has a great advantage over the LS method in that accurate algo-
 196 rithms for advecting F can be applied so that mass/volume is conserved up to
 197 machine precision while still maintaining a sharp representation of the interface.
 198 On the other hand, the disadvantage of the VOF method in comparison to the
 199 LS method is that tangled and difficult reconstruction procedures are required
 200 for determining the slope of the piecewise linear VOF reconstructed interface.
 201 In the LS method, the signed distance function ϕ (LS function) is used to track
 202 the interface. The interface is implicitly represented by the set of points in which
 203 $\phi = 0$. Liquid and gas regions are defined as $\phi > 0$ in the liquid and $\phi < 0$ in the
 204 gas, respectively. One of the advantages of the LS method is that one can track
 205 and represent smoothly the interface, but the LS method has the disadvantage
 206 that mass/volume is not explicitly conserved. In the CLSVOF method, the cou-
 207 pling between the LS function and the VOF function occurs when computing
 208 the normal of the reconstructed interface in the VOF calculation process and
 209 also when assigning the LS function with the exact signed normal distance to
 210 the reconstructed interface in the LS calculation process. That is to say, the
 211 piecewise linear approximation (the volume-of-fluid reconstruction step) for the
 212 VOF method is determined using the unit normal vector (\mathbf{n}) estimated from
 213 information of the LS function. By taking advantage of both methods, the evo-
 214 lution of the liquid-gas interface location can be computationally captured in
 215 such a way so that volume/mass is preserved to machine precision and at the
 216 same time, the interface normals and the surface tension force (which is pro-
 217 portional to the interface curvature) can be straightforwardly derived from the
 218 smooth level set function.

219 In our studies, the two-phase fluid flow is comprised of air and a viscous
 220 Newtonian liquid. The Heaviside function, $\mathcal{H}(\phi)$, which is defined as

$$\mathcal{H}(\phi) = \begin{cases} 1 & \phi \geq 0 \\ 0 & \phi < 0 \end{cases} \quad (3)$$

221 will be used below to distinguish each of the two fluids. A single set of three-
 222 dimensional equations governs the motion of both fluids, which are taken to be
 223 incompressible, and consists of the continuity equation and the Navier-Stokes
 224 equations with surface tension forces:

$$\nabla \cdot \mathbf{u} = 0 \quad (4)$$

$$\frac{\partial \mathbf{u}}{\partial t} + (\mathbf{u} \cdot \nabla) \mathbf{u} = \frac{1}{\rho} \nabla \cdot (-p \mathbf{I} + 2\mu \mathbf{D}) + \mathbf{g} - \frac{\sigma \kappa}{\rho} \nabla \mathcal{H} \quad (5)$$

225 \mathbf{u} is the velocity vector, t represents time, p is the pressure, \mathbf{I} is the unit ten-
 226 sor, \mathbf{D} is the rate of deformation tensor ($\mathbf{D} = \frac{1}{2}(\nabla \mathbf{u} + (\nabla \mathbf{u})^T)$), ρ is the density,
 227 μ is the viscosity, κ is the interfacial curvature, and the Heaviside function $\mathcal{H}(\phi)$

228 is a function of the level set (LS) function ϕ . The singular Heaviside gradient
 229 term in the right hand side of equation (5) is a body force representing the sur-
 230 face tension force and is equivalent to specifying that the jump in the normal
 231 stress is equal to $\sigma\kappa$ (Tanguy et al. [45]). The surface tension force expressed by
 232 the singular Heaviside gradient term acts only on the gas-liquid interface. The
 233 sharp interface ‘‘Ghost Fluid Method’’ (Kang et al. [19]) is used to discretize
 234 the gradient of the Heaviside function as it appears in the surface tension force
 235 term. This force, upon discretization, is only non-zero across cells in which the
 236 level set function changes sign.

237 The interfacial curvature κ is computed with second order accuracy directly
 238 from the volume-of-fluid (VOF) function and the level set function using the
 239 height function technique (Sussman [40], Sussman et al. [44]). We remark that
 240 we get the same results if we were to compute κ directly from the LS function
 241 using the ‘‘level set’’ height function technique.

242 Since ρ and μ are taken to be constant in each fluid, with a jump at the
 243 interface, they can be expressed in terms of the Heaviside function,

$$\rho = \rho_m \mathcal{H} + \rho_b (1 - \mathcal{H}), \quad \mu = \mu_m \mathcal{H} + \mu_b (1 - \mathcal{H}). \quad (6)$$

244 The subscripts ‘‘b’’ and ‘‘m’’ refer to ‘‘drop or bubble’’ and ‘‘matrix fluid’’,
 245 respectively. To represent the free surface with the CLSVOF method, we must
 246 evolve the solution to both the VOF equation for F and the LS equation for ϕ :

$$\frac{\partial F}{\partial t} + (\mathbf{u} \cdot \nabla) F = 0, \quad \frac{\partial \phi}{\partial t} + (\mathbf{u} \cdot \nabla) \phi = 0. \quad (7)$$

247 In all computations, the discretized variables p , ϕ and F are located at the
 248 cell centers and the discrete velocity variable \mathbf{u} is located at cell face centers.
 249 Our computations are performed using an overall second-order accurate hydro-
 250 dynamic scheme. The spatial discretization uses second-order accurate, slope-
 251 limited, upwind techniques for the nonlinear advective terms. The velocity and
 252 pressure fields are computed using an implicit pressure projection procedure.

253 The temporal discretization of our numerical method is an operator split
 254 projection method as described by Sussman et al. [44]. An outline of our method
 255 is as follows (see Sussman et al. [44], section 4, for more details):

All Steps. Timestep

256 The timestep, Δt , is governed by the CFL condition and surface tension
 257 (section 5.7 of Sussman et al. [44]):

$$\Delta t < \min_{i,j,k} \left(\frac{\Delta x}{2|U^n|}, \frac{1}{2} \sqrt{\frac{\rho^L}{8\pi\sigma}} \Delta x^{3/2} \right)$$

Step 1. CLSVOF interface advection

$$\begin{aligned} \phi^{n+1} &= \phi^n - \Delta t [\mathbf{u} \cdot \nabla \phi]^n \\ F^{n+1} &= F^n - \Delta t [\mathbf{u} \cdot \nabla F]^n \end{aligned}$$

Step 2. Nonlinear advective force terms

$$\mathcal{A} = [\mathbf{u} \cdot \nabla \mathbf{u}]^n$$

Step 3. Viscosity force

$$\frac{\mathbf{u}^* - \mathbf{u}^n}{\Delta t} = -\mathcal{A} + g\vec{z} - [\nabla p/\rho]^n + \frac{1}{2} \frac{\nabla \cdot (2\mu \mathbf{D}^n) + \nabla \cdot (2\mu \mathbf{D}^*)}{\rho}$$

²⁵⁸ **Step 4. Pressure projection and ghost fluid surface tension algorithm**

$$\mathbf{V} = \mathbf{u}^n + \Delta t(-\mathcal{A} + g\vec{z} + \frac{1}{2} \frac{\nabla \cdot (2\mu \mathbf{D}^n) + \nabla \cdot (2\mu \mathbf{D}^*)}{\rho})$$

²⁵⁹

$$\mathbf{V} = \mathbf{V} - \Delta t \frac{\sigma \kappa(\phi^{n+1})}{\rho} \nabla \mathcal{H}(\phi^{n+1})$$

²⁶⁰

$$\nabla \cdot \frac{\nabla p}{\rho} = \frac{1}{\Delta t} \nabla \cdot \mathbf{V}$$

²⁶¹

$$\mathbf{u}^{n+1} = \mathbf{V} - \Delta t \frac{\nabla p}{\rho}$$

²⁶² To make efficient use of computational resources, our numerical simulations
²⁶³ utilize an adaptive hierarchy of grids based on a dynamic adaptive mesh refine-
²⁶⁴ ment (AMR) technique (Sussman et al. [41]). Adaptive grids are dynamically
²⁶⁵ adjusted based on the location of the deforming gas-liquid interface. In the
²⁶⁶ AMR technique, the grid resolution is increased in regions near the interface
²⁶⁷ while a coarser grid is used where the flow is relatively steady. The upper panel
²⁶⁸ of Figure 1(b) displays a schematic view of the hierarchical grid structure and
²⁶⁹ the lower panel corresponds to an actual computational example corresponding
²⁷⁰ to bubble deformation in simple linear shear flow. In general, the mesh hier-
²⁷¹ archy is composed of different levels of refinement ranging from coarsest $\ell = 0$
²⁷² (“level-0”) to finest $\ell = \ell_{\max}$ (“level- ℓ_{\max} ”). The refinement ratio of one grid
²⁷³ size ($\Delta x = \Delta y = \Delta z$) to the next finer level is two so that $\Delta x^{\ell+1} = 0.5 \Delta x^\ell$. All
²⁷⁴ computations in this study used an AMR system with a maximum prescribed
²⁷⁵ level $\ell_{\max} = 1$ (as illustrated in the upper panel of Figure 1(b)). In our adaptive
²⁷⁶ mesh refinement algorithm, the velocity in the coarse grid cells that neighbor
²⁷⁷ fine grid cells is interpolated from the coarse grid using bilinear interpolation in
²⁷⁸ order to initialize “ghost” fine cells. Thus, the bilinear interpolation procedure
²⁷⁹ produces interpolated fine grid data as a linear combination of the coarse grid
²⁸⁰ data.

281 3.2. Validation of the numerical method

282 The effectiveness of our computational method has been demonstrated for
 283 the complicated rising motion of single bubbles and drops in viscous liquids
 284 Ohta and Sussman [29], Ohta et al. [26, 27]. In this section, the accuracy of
 285 our computational method will be verified for the problem of shear-induced
 286 deformation of a drop and bubble. First, we compare quantitatively against
 287 the steady-state drop deformation results reported by Li et al. [24]. The shape
 288 of a deformed drop in simple linear shear flow is described in terms of the Taylor
 289 deformation parameter $D = (a - b)/(a + b)$, where a and b are the major and minor
 290 axes of the deformed drop respectively. For consistency, we perform numerical
 291 simulations using CLSVOF over the same computational domain and grid size
 292 used in Li et al. [24], which has dimensions $L(8R) \times W(4R) \times H(8R)$ (recall that
 293 R is the bubble/drop radius) and a level-0 grid size $\Delta x = \Delta y = \Delta z = R/8$; our
 294 two-level AMR grid structure also uses a finer level-1 grid size $\Delta x^{\ell=1} = \Delta y^{\ell=1} =$
 295 $\Delta z^{\ell=1} = R/16$. Numerical results are listed in Table 1 for D as a function of
 296 Re , with $Ca = 0.3$ and $\lambda = \eta = 1$ fixed in every case. The results in Table 1
 297 compare computations using our CLSVOF algorithm with corresponding results
 298 that were obtained with the VOF method used in Li et al. [24].

Table 1: Comparison of the Taylor deformation parameter D for a drop as a function of Re ($Ca = 0.3$, $\lambda = \eta = 1$). In all cases, the domain size is $L(8R) \times W(4R) \times H(8R)$, where R is the drop radius. The CLSVOF method computations used a two-level AMR computational domain with a level-0 discretization $\Delta x^{\ell=0} = \Delta y^{\ell=0} = \Delta z^{\ell=0} = R/8$ and a level-1 discretization $\Delta x^{\ell=1} = \Delta y^{\ell=1} = \Delta z^{\ell=1} = R/16$.

Reynolds number	0.1	0.5	0.6	0.75
D (Li et al. [24])	0.3968	0.45	0.4768	Breakup
D (Our study)	0.3960	0.4570	0.4758	Breakup

298 Next, we examine the validation of our computational method in which
 299 we compare with the “bubble deformation in simple linear shear flow” results
 300 reported by Müller-Fischer et al. [25]. Müller-Fischer et al. [25] experimentally
 301 inquired into the bubble deformation under the condition of $Re \approx 0$. In our
 302 study, we computed the bubble deformation on a computational domain with
 303 dimensions $L(12R) \times W(6R) \times H(6R)$ and a computational grid in which the
 304 finest level grid size was $\Delta x^{\ell=1} = \Delta y^{\ell=1} = \Delta z^{\ell=1} = R/16$. Computations
 305 were performed for the conditions of $Ca = 0.96$ and $Ca = 1.63$ with $Re \approx 0$
 306 ($Re = 5.0 \times 10^{-4}$), $\lambda = 1.2 \times 10^{-3}$ and $\eta \leq 1.2 \times 10^{-6}$. The prescribed parameters
 307 are consistent with the experimental conditions by Müller-Fischer et al. [25].
 308 Comparisons of our numerical results and previous experimental results (Müller-
 309 Fischer et al. [25]) are tabulated in Table 2. Additionally, in Table 2, we also list
 310 experimental results with the condition of $Re \approx 0$ and $\lambda \approx \eta \approx 0$ by Rust and
 311 Manga [37]. These experimental values were obtained from the graph showing
 312 the relation of D vs Re (Rust and Manga [37]). As is clear from Table 2, our
 313 numerical results predicted larger values of D than experimental ones reported
 314 by Müller-Fischer et al. [25]. Nevertheless, our numerical results are very close to
 315 by Müller-Fischer et al. [25]. Nevertheless, our numerical results are very close to

316 the experimental results by Rust and Manga [37], which emphasizes the intrinsic
 317 difficulties associated with experimental investigations of bubble dynamics, even
 318 in simple linear shear flow. These comparisons suggest that our computational
 319 method is effective and robust at reproducing bubble dynamics in simple linear
 shear flow.

Table 2: Comparison of D for a bubble as a function of Ca ($Re \approx 0$, $\lambda \approx \eta \approx 0$). In all cases, the domain size is $L(12R) \times W(6R) \times H(6R)$. The CLSVOF computations used a two-level AMR computational domain with a level-0 discretization $\Delta x^{\ell=0} = \Delta y^{\ell=0} = \Delta z^{\ell=0} = R/8$ and a level-1 discretization $\Delta x^{\ell=1} = \Delta y^{\ell=1} = \Delta z^{\ell=1} = R/16$.

Capillary number	0.96	1.63
D (Müller-Fischer et al. [25])	0.37	0.58
D (Rust and Manga [37])	0.71 ± 0.05	0.81 ± 0.02
D (Our study $\Delta x^{\ell=1} = R/16$)	0.63	0.71

320

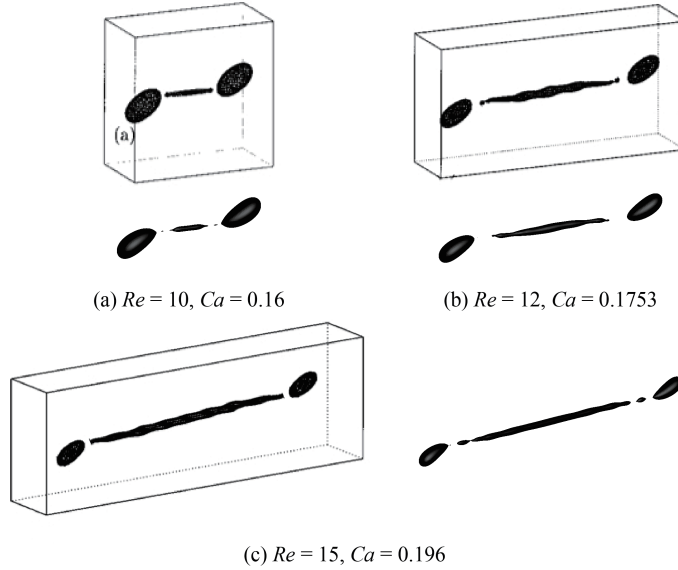


Figure 2: Comparison with results reported in Renardy and Cristini [36] (shown in boxes) for drop breakup in shear flow. In Renardy and Cristini [36], the computational domain dimensions were $W = 4R$, $H = 8R$, and L was varied depending on the Re and Ca conditions. The grid size in Renardy and Cristini [36] was set to $\Delta x = \Delta y = \Delta z = R/8$. Reprinted with permission from reference Renardy and Cristini [36]. Copyright 2001, AIP Publishing. The results obtained with our CLSVOF algorithm, corresponding to each case in reference Renardy and Cristini [36], are shown outside boxes. The CLSVOF method used a two-level AMR computational domain with a level-0 discretization $\Delta x^{\ell=0} = \Delta y^{\ell=0} = \Delta z^{\ell=0} = R/8$ and a level-1 discretization $\Delta x^{\ell=1} = \Delta y^{\ell=1} = \Delta z^{\ell=1} = R/16$. The onset of drop breakup is demonstrated for (a) $Re = 10$, $Ca = 0.16$, (b) $Re = 12$, $Ca = 0.1753$, and (c) $Re = 15$, $Ca = 0.196$. For all three Re and Ca conditions, $\lambda = \eta = 1$.

Finally, we present a comparison with numerical results for drop breakup reported in Renardy and Cristini [36]. Figure 2 demonstrates drop breakup with pinch-off behavior for three Re and Ca conditions and with constant values of $\lambda = \eta = 1$ for all cases. The three cases that we consider correspond to (a) $Re = 10, Ca = 0.16$, (b) $Re = 12, Ca = 0.1753$, and (c) $Re = 15, Ca = 0.196$, and which are illustrated in Figures 2(a)-(c), respectively. The results reported in Renardy and Cristini [36], which were obtained with a VOF method, are shown inside boxes while results obtained with our CLSVOF approach are displayed outside boxes. In the computations presented in Renardy and Cristini [36], the dimensions $W = 4R$ and $H = 8R$ were fixed, while L was changed depending on Re and Ca conditions, and the grid size was set to $\Delta x = \Delta y = \Delta z = R/8$. To compare with their results, we performed simulations with the CLSVOF method over a two-level AMR computational domain of the same dimensions and the same level-0 discretization: $\Delta x^{\ell=0} = \Delta y^{\ell=0} = \Delta z^{\ell=0} = R/8$; we set the finer level-1 grid size $\Delta x^{\ell=1} = \Delta y^{\ell=1} = \Delta z^{\ell=1} = R/16$. The results shown in Figure 2 verify that our numerical approach can reproduce the same drop breakup behavior presented in Renardy and Cristini [36]. Slight differences between the results can be attributed to the increased resolution used in our study in the level-1 grid around the elongated drop.

The numerical validation studies performed in this section and the following section demonstrate that our numerical method can reliably determine the transition regions at which shear-induced bubble or drop deformation leads to breakup. We remark that in the next section, we demonstrate that we can expect an error of 3% for predicting the transition to break-up. The analysis in this section and the following also demonstrate that the error is reduced by a factor of 2 each time the grid is refined by a factor of 2. Also, we refer the reader to Ohta et al. [28] in which we apply our CLSVOF method for bubble formation problems.

349 3.3. Consideration of domain and grid sizes

350 3.3.1. Selecting the appropriate domain size

The computational domain size used in numerical studies can affect the behavior of drop deformation and breakup. Referring to Figure 1(a), with an appropriately large domain length L and a fixed width $W = 4R$, the effect of the height H on drop behavior was examined in Li et al. [24] for Stokes flows and various Ca conditions and in Komrakova et al. [21] for $Re = 1$ and $Ca = 0.27$. Other related studies investigated drop breakup sensitivity (Renardy and Cristini [34]) and drop deformation sensitivity (Renardy et al. [35]) with respect to the entire domain size.

Here we investigate the drop dynamics sensitivity to domain size around the critical Reynolds number $Re_c = 0.75$. Specifically, we consider domain size sensitivity for the condition of $Re = 0.75, Ca = 0.3$, and $\lambda = \eta = 1$, which is a condition used in the comparison studies of the previous section. As shown in Table 1, the drop breaks up for the condition of $Re = 0.75$ and $Ca = 0.3$ with a domain size of $L(8R) \times W(4R) \times H(8R)$. Results for domain size sensitivity

Table 3: Comparison of the Taylor deformation parameter D for a drop as a function of domain size ($Re = 0.75$, $Ca = 0.3$, $\lambda = \eta = 1$). CLSVOF method computations used a two-level AMR computational domain with a level-0 discretization $\Delta x^{\ell=0} = \Delta y^{\ell=0} = \Delta z^{\ell=0} = R/8$ and a level-1 discretization $\Delta x^{\ell=1} = \Delta y^{\ell=1} = \Delta z^{\ell=1} = R/16$.

System	Domain size ($L \times W \times H$)	D
System 1	$8R \times 4R \times 8R$	Breakup
System 2	$12R \times 4R \times 8R$	Breakup
System 3	$8R \times 4R \times 6R$	0.541
System 4	$8R \times 6R \times 6R$	0.466
System 5	$8R \times 8R \times 8R$	0.460
System 6	$8R \times 16R \times 16R$	0.460

for six domain systems, all of which use a level-1 grid size $\Delta x^{\ell=1} = \Delta y^{\ell=1} = \Delta z^{\ell=1} = R/16$, are tabulated in Table 3. Note that the domain size used in the comparison study (Table 1) corresponds to System 1.

The results in Table 3 suggest that drop deformation is promoted when we use a domain size with $W = 4R$. In contrast, the drop does not break up and becomes stable with a deformed shape if we set L large enough and $W \geq 6R$ and $H \geq 6R$. Since the value of D for the domain size $L(8R) \times W(6R) \times H(6R)$ differs by only 1.3% with the value for the domain size of $L(8R) \times W(16R) \times H(16R)$, in the results that follow we set the width to $W = 6R$ and the height to $H = 6R$ to minimize the number of computational grid nodes along those directions. To determine the critical Reynolds number Re_c (with $Ca = 0.3$), we consider a domain size of $L(24R) \times W(6R) \times H(6R)$, and we find that the drop reaches a stable state with deformation parameter $D=0.549$ for $Re = 1.0$, while a value of $Re = 1.1$ leads to drop breakup.

3.3.2. Selecting the appropriate grid size

The grid size and adaptive meshing strategy that we adopt is chosen in order to answer the research question as to the conditions which determine whether a bubble in shear flow will break-up or not. In such a case, we must accurately capture the balance of forces with respect to the (non-local) force exerted from the wall driven flow acting against the interfacial surface tension force. The accuracy of the “Critical Reynolds Number” depends on the largest Taylor Deformation parameter D that is supported by the grid (see e.g. Figures 8 and 11). As we report here, we have found that as long as the grid size is fine enough to support a Taylor Deformation parameter $D < 0.95$, then the transition region (i.e. “Critical Reynolds number”) (see Figures 3 and 12) will be captured with a tolerance of three percent. The simulation time becomes impractical if we were to try to further improve the “critical Reynolds number” accuracy. A smaller tolerance would necessitate a larger supported Deformation parameter D which would in turn necessitate a higher aspect ratio computational domain, increased droplet surface area at break-up, increased number of time steps, and higher resolution for representing the drop/bubble at its thinnest point.

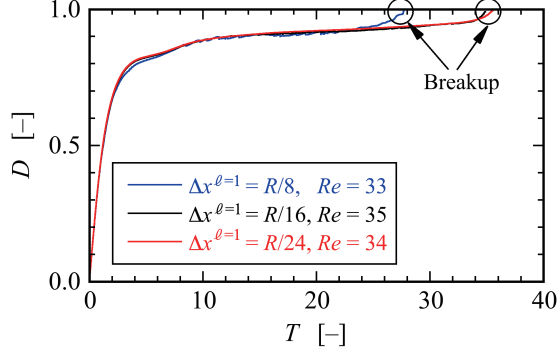


Figure 3: Time evolution of the deformation parameter D versus dimensionless time $T = \Gamma t$ for a bubble, obtained with three grid systems at different resolutions. All three resolutions use a two-level AMR grid with an effective fine resolution grid size $\Delta x^{\ell=1} = \Delta y^{\ell=1} = \Delta z^{\ell=1}$. The evolution of D using the first system, where $\Delta x^{\ell=1} = R/8$, is shown in blue and it predicts that bubble breakup occurs at a Reynolds number $Re = 33$. The evolution of D using the second system, where $\Delta x^{\ell=1} = R/16$, is shown in black and it predicts that bubble breakup occurs at a Reynolds number $Re = 35$. Results with the third system, shown in red, use $\Delta x^{\ell=1} = R/24$, and they predict that breakup occurs at $Re = 34$. The capillary number corresponding to these results is $Ca = 1.0$. ($\lambda = 1.2 \times 10^{-3}$, $\eta < 1.0 \times 10^{-3}$)

396 We make the distinction between our present research, and the research
 397 found in the work of Zhang et al. [55, 56] on predicting the conditions for bubble
 398 mergers. Even in the most extreme cases for mergers, the largest Deformation
 399 parameter never exceeds 0.4 in Zhang et al. [55]. In summary, our gridding
 400 requirements necessitate grid points distributed relatively evenly throughout the
 401 computational domain when a bubble is stretched to a $D = 0.9$ Deformation,
 402 whereas in Zhang et al. [55] the gridding strategy necessitates a more localized
 403 strategy.

404 The numerical results presented in this and the previous section used a
 405 finest-level grid size set to $\Delta x^{\ell=1} (= \Delta y^{\ell=1} = \Delta z^{\ell=1}) = R/16$. To verify the
 406 adequacy of this grid resolution, we present grid refinement results for a bubble
 407 breakup simulation with $Ca = 1.0$, which corresponds to the most deformable
 408 and stretchable bubble case considered in our numerical studies. We use three
 409 different grid systems, (i) $\Delta x^{\ell=1} = R/8$, (ii) $\Delta x^{\ell=1} = R/16$, and (iii) $\Delta x^{\ell=1} =$
 410 $R/24$, in order to determine Re_c . Figure 3 shows the time evolution of the
 411 deformation parameter D over time for the three grid systems; the x -axis is a
 412 dimensionless time defined by $T = \Gamma t$ and the y -axis is D . The results show that
 413 bubble breakup occurs at $Re_c = 35$ for the grid system with $\Delta x^{\ell=1} = R/16$,
 414 while the finer computational grid with $\Delta x^{\ell=1} = R/24$ predicts a critical value of
 415 $Re_c = 34$. For the $\Delta x^{\ell=1} = R/8$ results, it is clear that the $R/8$ resolution is too
 416 coarse in order to capture the proper break-up time, albeit the critical Reynolds'
 417 number, $Re_c = 33$, was still close to the finer grid resolution cases. Note that
 418 although the time evolution of D for the two finer resolution systems ($R/16$ and
 419 $R/24$) is consistent between the two, (the predicted critical Reynolds numbers

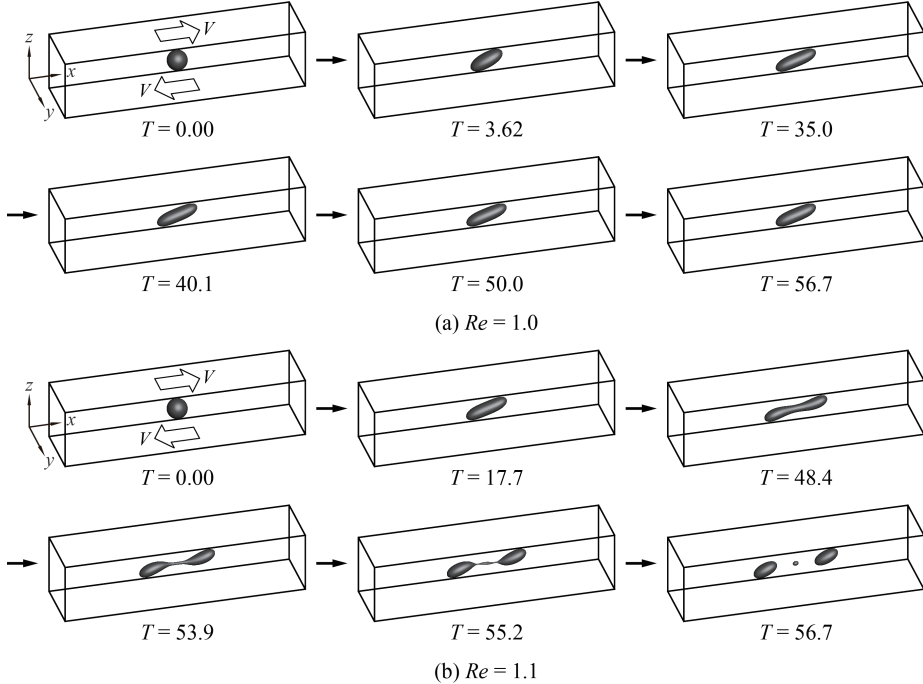


Figure 4: Time evolution of drop deformation and breakup in shear flow at the condition of $Ca = 0.3$ with (a) $Re = 1.0$ and (b) $Re = 1.1$. The “drop” critical Reynolds number corresponding to $Ca = 0.3$ is $1.0 < Re_c < 1.1$. ($\lambda = \eta = 1.0$)

differ by $\sim 3\%$), the computational time using the grid system with $\Delta x^{\ell=1} = R/24$ was more than 6 times longer than the one based on the coarser system with $\Delta x^{\ell=1} = R/16$. We remark that in our search for Re_c , we considered a wide range of values of Ca and we found it necessary to use a large L ($\sim 24R$) since for certain shear flows the bubble can stretch significantly without breaking up. Nevertheless, for the conditions presented in this section, the results indicate that our numerical approach, even with a finest-level resolution set to $\Delta x^{\ell=1} = R/16$, is capable of accurately reproducing bubble deformation and breakup without sacrificing any essential dynamical features.

4. Results and Discussion

4.1. Drop deformation and breakup

To illustrate the differences in deformation and breakup between a drop and a bubble around critical conditions, we first present numerical results for drop deformation. The time evolution of drop deformation and breakup in simple linear shear flow for two conditions is shown in Figure 4; the first case, shown in Figure 4(a), uses $Ca = 0.3$ and $Re = 1.0$, while the second case, depicted in Figure 4(b), uses $Ca = 0.3$ and $Re = 1.1$. Using a domain size of

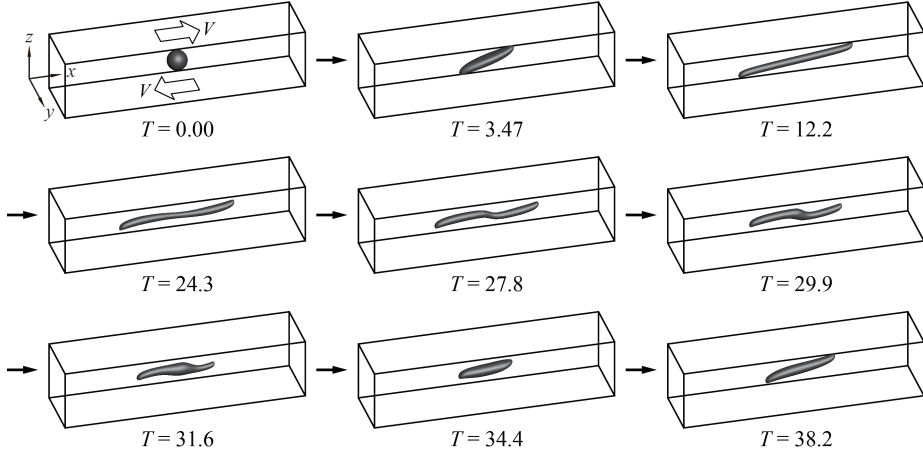


Figure 5: Time evolution of bubble deformation in shear flow at the condition of $Ca = 0.3$ and $Re = 92$. The “bubble” critical Reynolds number corresponding to $Ca = 0.3$ is $92 < Re_c < 93$. In contrast to the drop deformation case, when Re is slightly below Re_c (See Figure 4.1 $Re = 1.0$ for the drop case), the bubble shape will not reach a steady shape, instead the bubble shape alternates between the shapes “slightly stretched” ($T = 3.47$), fully stretched and “doglegged” ($T = 27.8$) and “almost” back to the original “slightly stretched” case ($T = 34.4$). ($\lambda = 1.2 \times 10^{-3}$, $\eta < 1.0 \times 10^{-3}$)

437 $L(24R) \times W(6R) \times H(6R)$, in the case with $Re = 1.0$, the drop gradually deforms
 438 and finally attains a stable deformed state. After $T = 35.0$, the drop remains a
 439 **stable deformed state with $D = 0.549$** . Over the same domain, for the case with
 440 $Re = 1.1$, the “mother” drop elongates over time and the volume at the ends
 441 of the deforming drop expands; that is, both ends of the drop become bulb-
 442 shaped. As time progresses, particularly over the time interval $48.4 \leq T \leq 55.2$,
 443 a thread-bridge forms between the bulbous ends and the thread-bridge becomes
 444 thinner. Finally, at around the dimensionless time $T \sim 56.7$, the mother drop
 445 breaks up, forming two “daughter” drops through the pinch off; one satellite
 446 drop is also generated between the pinched off daughter drops.

447 4.2. Bubble deformation and breakup

448 Next we present numerical results that illustrate the conditions that lead
 449 to bubble deformation without breakup as well as conditions where the bubble
 450 deforms and ultimately breaks up. The time evolution of shear-induced bubble
 451 deformation without breakup at the condition of $Ca = 0.3$ and $Re = 92$ is
 452 depicted in Figure 5 and the bubble breakup process with flow condition of
 453 $Ca = 0.3$ and $Re = 93$ is illustrated in Figure 6. The results indicate that
 454 the critical Reynolds number is approximately $Re_c = 93$ (with $Ca = 0.3$).
 455 A comparison with the drop breakup dynamics presented in Section 4.1 and
 456 the corresponding processes for bubble deformation and breakup exhibit very
 457 distinct features. First, we note that a relatively large shear force magnitude is
 458 required for bubble breakup ($\lambda = 1.2 \times 10^{-3}$, $\eta < 1.0 \times 10^{-3}$) compared with the

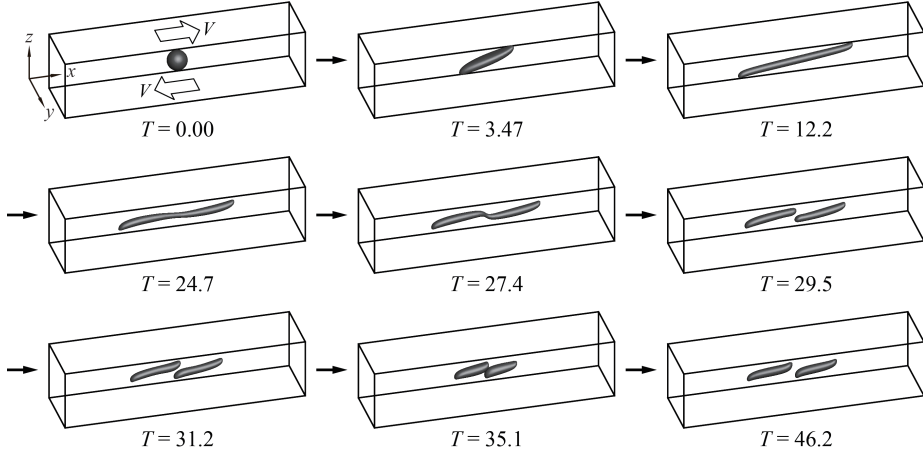


Figure 6: Time evolution of bubble deformation in shear flow at the condition of $Ca = 0.3$ and $Re = 93$. The “bubble” critical Reynolds number corresponding to $Ca = 0.3$ is $92 < Re_c < 93$. ($\lambda = 1.2 \times 10^{-3}$, $\eta < 1.0 \times 10^{-3}$)

case of the drop ($\lambda = \eta = 1$). Then, for the same value of $Ca = 0.3$, the critical Reynolds number for the bubble is around 85 times larger than that for the drop. Focusing on the bubble dynamics with no-breakup (Figure 5), the results show that the bubble is largely elongated in the x -direction at the early stages ($T \leq 24.3$) of bubble deformation, but the bubble does not develop the bulb-like shape (large volume areas) at both ends present in the drop deformation process. It is also evident that the ends of the deforming bubble develop cusped shapes under the influence of the strong shear flow. In providing a more detailed description, very large shear forces are required to deform the bubble because $\lambda \simeq 0$ and $\eta \simeq 0$. Thus, the bubble undergoing large shear forces at $T > 0$ is largely stretched long the shear flow direction, and the very long elongated bubble with cusped shapes is formed. Accordingly, the bubble finally breaks up through f the elongated shape without forming a bulb-like shape. A noteworthy feature for the non-breaking bubble is that it does not settle into a deformed stable state as in the case of drop deformation presented in Figure 4.1(a). After an initial elongation process, the bubble enters a shrinking phase ($T = 27.8$) where the doglegged shape formed at the center of the bubble returns to a smaller deformed shape ($T = 34.4$) that is similar to its earlier shape ($T = 34.7$). However, when we compare the early deformed bubble shape at $T = 34.7$ with the shape at $T = 34.4$, it is clear that the shapes are not identical. Following the shrinking phase, the bubble begins to stretch again ($T = 38.2$) and the bubble oscillates between its elongated shape and shortened geometry.

For the case of bubble breakup (Figure 6), we observe that the deformation process is almost the same as the no-breakup case until the doglegged shape is formed at $T \sim 27.4$. The bubble finally breaks during the time interval $27.7 \leq T \leq 29.5$. For a closer examination of the bubble breakup process,

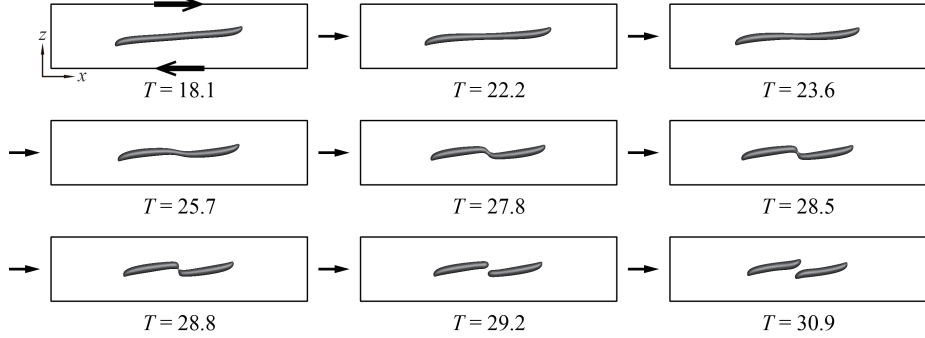


Figure 7: Detail of bubble breakup process in shear flow at the condition of $Ca = 0.3$ and $Re = 93$. The “bubble” critical Reynolds number corresponding to $Ca = 0.3$ is $92 < Re_c < 93$. ($\lambda = 1.2 \times 10^{-3}$, $\eta < 1.0 \times 10^{-3}$)

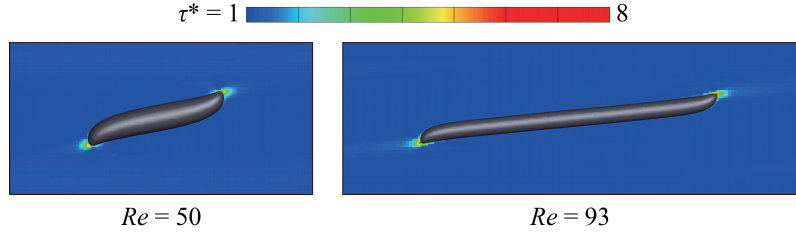


Figure 8: Normalized shear stress τ^* around a bubble for two Reynolds numbers under the condition of $Ca = 0.3$. The left image shows the shear stress profile at $Re = 50$ and the right image at $Re = 93$.

485 a detailed panel of cross-sectional slices in the xz -plane through the bubble
 486 shape center is presented in Figure 7. The images displayed in Figure 7, which
 487 are taken at shorter time intervals than those shown in Fig. 6, reveal that the
 488 bubble breaks up into two daughter bubbles due to the pinch off at the thread-
 489 bridge part of the doglegged shape during the shrinking process ($T = 28.5 \sim$
 490 28.8). After breaking up, the two daughter bubbles migrate to the center: the
 491 left daughter bubble moves toward the right-side of the domain and the right
 492 daughter bubble moves to the left side (see results for $T = 29.5 \sim 35.1$ in
 493 Figure 6 and for $T = 28.8 \sim 30.9$ in Figure 7). The two daughter bubbles then
 494 momentarily congregate near the domain center ($T = 35.1$ in Figure 6), before
 495 they slowly start to separate: the left daughter bubble moves to the left and the
 496 right daughter bubble moves to the right ($T = 46.2$ in Figure 6). The results
 497 clearly demonstrate that the bubble breakup process is markedly different from
 498 the analogous drop breakup process with $\lambda = 1$ and $\eta = 1$. Note that the
 499 appearance of deformation and breakup of the drop will largely depend on the
 500 viscosity ratios.

501 4.3. Shear stress acting on the bubble

502 In the previous section, the appearance of bubble deformation and breakup
503 was discussed. It is expected that a large deformation and breakup of the bubble
504 are closely related to the state of shear stress acting on the bubble. Figure 8
505 shows the shear stress profile around a bubble for two Reynolds numbers under
506 the condition of $Ca = 0.3$: Reynolds number equal to 50 and 93. The shear
507 stress profile on the left corresponds to the case of $Re = 50$ and the right side
508 shows the shear stress profile for the case of $Re = 93$. The normalized shear
509 stress, $\tau^* = \tau/\tau_0$, is defined as a ratio of the local shear stress $\tau = \mu_m \sqrt{2\mathbf{D} : \mathbf{D}}$
510 and the apparent shear stress $\tau_0 = \mu_m \Gamma$. In this study, for a given Ca condition,
511 the same value of τ_0 is used regardless of Re . For the case of $Re = 50$, the bubble
512 reached a deformed stable state, **and the shear stress profile around the bubble
513 was drawn after the bubble attained a stable deformed state.** As observed
514 in previous sections, when the value of Re is slightly below the critical Re
515 condition, the bubble does not settle into a deformed stable state but instead
516 alternates in an elongation and contraction process. **The shear stress profile for
517 the case of $Re = 93$ was depicted when the bubble sufficiently elongated ($T =$
518 14.9).** In comparison to the $Re = 50$ case on the left, the right image in Fig. 8
519 ($Re = 93$) shows a higher shear stress profile near the bubble endpoints as it
520 undergoes an elongation state in the process toward breakup. The value of the
521 maximum shear stress for the case of $Re = 50$ is $\tau^* \approx 6$ and the maximum shear
522 stress for the case of $Re = 93$ at the moment shown in Fig. 8 has the value of
523 $\tau^* \approx 8$. The shear stress profile in Fig. 8 (color contour) is drawn in the range
524 from $\tau^* = 1$ to $\tau^* = 8$, but, for emphasis, shear stress regions with $\tau^* \geq 6$ are
525 illustrated in red. As can be seen in the figure, the strongest shear stresses are
526 concentrated on the ends of the bubble for both Re conditions. This indicates
527 that the strong shear stresses acting on the ends of the bubble are responsible
528 for much of the bubble stretching. It is important to note that the magnitude
529 of the shear stress acting on the ends of the bubble for the case of $Re = 93$ is
530 much larger than that for the case of $Re = 50$.

531 We also observe that the shear stress inside the bubble was very small relative
532 to that of the matrix fluid due to very small density and viscosity of the bubble.
533 Since the force of strong shear stresses acting on the ends of the bubble is
534 difficult to transfer across the interface, as a consequence, a sufficiently large Re
535 condition is required for large bubble deformations.

536 In summary, what we discover is that for the Reynolds number sufficiently below
537 the critical value, a relatively quick unsteady elongation period gives way to a
538 steady state (with no break up). On the other hand for Reynolds number close
539 to the critical Reynolds number, there is a prolonged, unsteady, elongation
540 period, in which periodic motion is observed and the deformation parameter
541 D is close to one. The “vacillating” behavior cannot last forever, ultimately
542 (perhaps stochastically!), the bubble will either settle down or break. We assert
543 that regardless of the outcome, this vacillating behaviour will always occur in
544 close proximity to the critical Reynolds’ number. In other words, regardless of
545 the outcome, we claim, using the grid resolution of $R/16$, that one is assured
546 of being within 3 percent of the critical Reynolds number (see Figure 3). In

547 fact, we hypothesize that there will always be “vacillating” behavior if one is
 548 sufficiently close to the critical Reynolds number. i.e. given an almost infinite
 549 supply of computational resources, as one hones in closer and closer to the
 550 critical Reynolds number, a “tug of war” will be observed between the surface
 551 tension force trying to pull the bubble together versus the wall driven shear
 552 stress trying to pull the bubble apart.

553 *4.4. Velocity field outside and inside the breaking bubble*

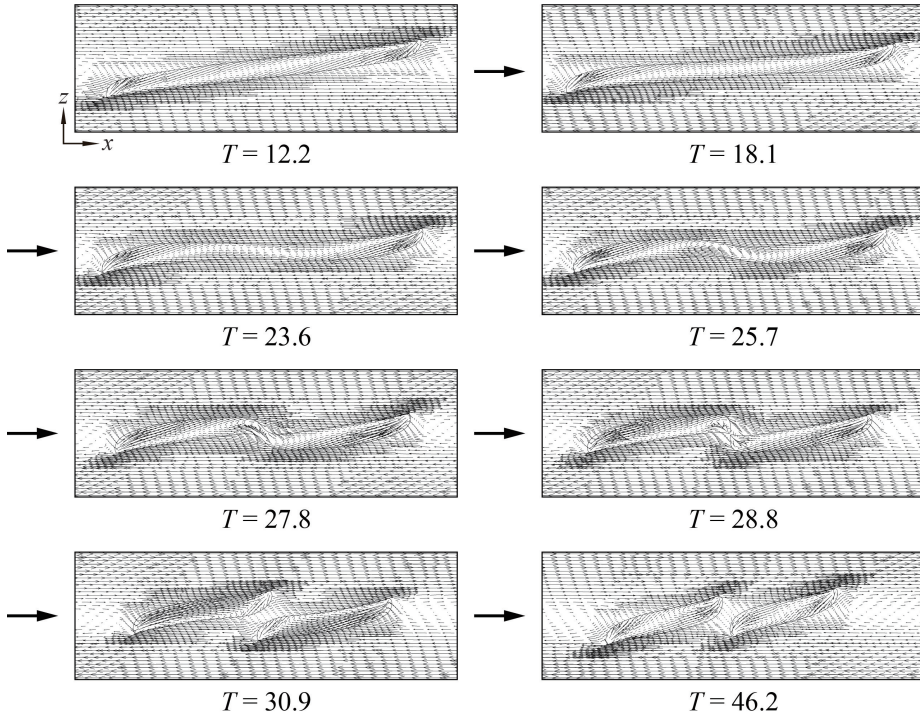


Figure 9: Fluid velocity field outside and inside the breaking bubble in shear flow at the condition $Ca = 0.3$ and $Re = 93$. The “bubble” critical Reynolds number corresponding to $Ca = 0.3$ is $92 < Re_c < 93$. ($\lambda = 1.2 \times 10^{-3}$, $\eta < 1.0 \times 10^{-3}$)

554 In this section, we consider the fluid flow velocity field outside and inside the
 555 bubble during the shear-induced breakup process. Detailed velocity fields of the
 556 deforming and breaking drop have already been presented in some references
 557 (Li et al. [24], Renardy and Cristini [34]). The velocity fields for the drop and
 558 the bubble will be influenced by the behavior of the breakup process, so the
 559 velocity fields for the drop and the bubble are not similar. Figure 9 shows the
 560 velocity fields outside and inside the bubble at cross-sectional slices in the xz -
 561 plane for a flow condition of $Ca = 0.3$ and $Re = 93$. Regions around the bubble
 562 where there is a higher density of velocity vectors correspond to the level-1 grid
 563 portion of the AMR structure. The simulation results show that the velocity

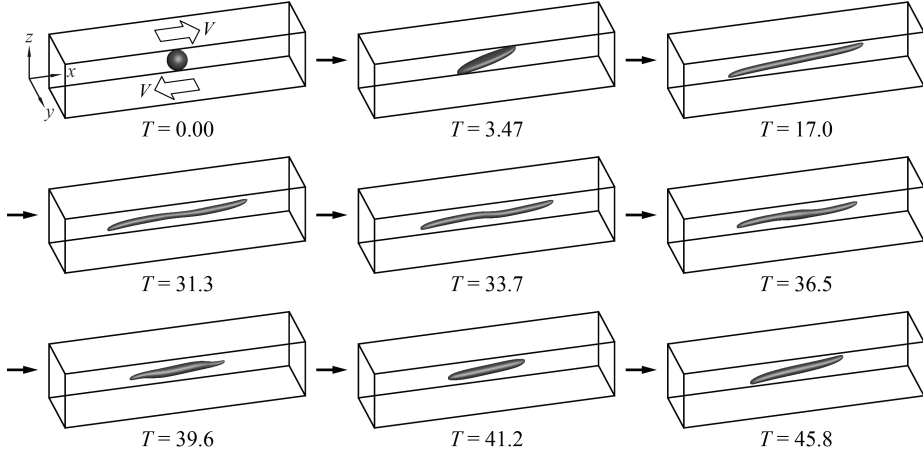


Figure 10: Time evolution of bubble deformation in shear flow at the condition of $Ca = 0.8$ and $Re = 42$. The “bubble” critical Reynolds number corresponding to $Ca = 0.8$ is $42 < Re_c < 43$. ($\lambda = 1.2 \times 10^{-3}$, $\eta < 1.0 \times 10^{-3}$)

field inside the bubble is particularly distinct from the surrounding flow field in the exterior of the bubble. The cross-sections at $T = 12.2$ and $T = 18.1$, taken during the elongation phase, show how shear forces at the lower and upper halves of the bubble act along the bottom and top surfaces, respectively, to deform the interface. Near the left and right edges of the bubble, inward interior flows (that point toward the bubble center) begin to develop. Strong shearing forces in the exterior near the bottom-left-end and top-right-end of the bubble interact with the interior flow field through the boundary to create cusped shapes at the bottom-left and top-right ends of the bubble while the interface is laterally elongated in the x -direction. During the shrinking process, which occurs for $23.6 \leq T \leq 27.8$, inward flows within the bubble extend over a wider region and are no longer localized near the bubble edges. Then, we observe that circulating flows form at the thread-bridge part of the doglegged bubble shape over the time interval [25.7, 27.8]. During the breakup process ($T \sim 28.8$), higher-intensity inward flows are formed inside the bubble, near the pinch off region, that are naturally larger than the surrounding interior flows and which are inextricably associated with the bubble migration illustrated in Figs. 6 and 7. As time proceeds further ($T = 46.2$), distinct inward flows are formed inside the daughter bubbles; the bubbles then begin their migration toward the side walls. Considering the left daughter bubble, for example, we see that the mechanism responsible for this movement results from larger shear forces acting on the bottom-left end than those in the top-left end.

4.5. Effect of surface tension on bubble deformation and breakup

In previous sections, we considered numerical simulations of bubble deformation and breakup with a capillary number $Ca = 0.3$. Here, we examine

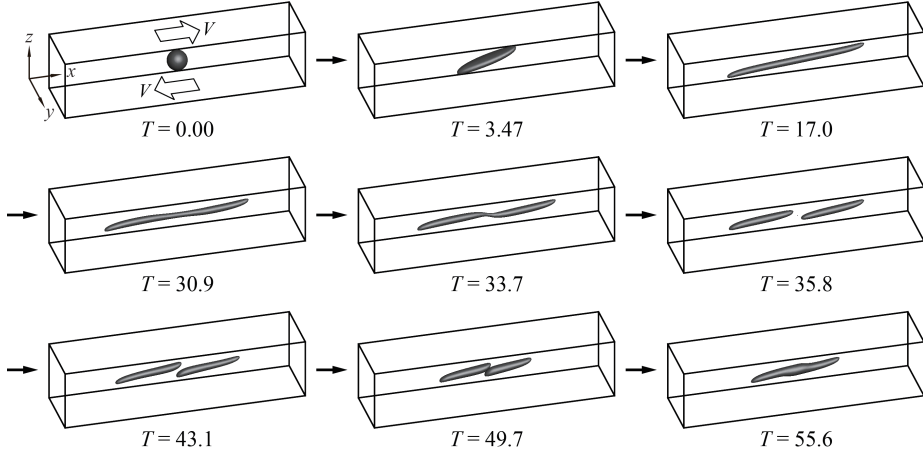


Figure 11: Time evolution of bubble deformation in shear flow at the condition of $Ca = 0.8$ and $Re = 43$. The “bubble” critical Reynolds number corresponding to $Ca = 0.8$ is $42 < Re_c < 43$. ($\lambda = 1.2 \times 10^{-3}$, $\eta < 1.0 \times 10^{-3}$)

similar bubble dynamics with $Ca = 0.8$ and we also investigate the effect of interfacial tension on bubble deformation and breakup. Using $Ca = 0.8$ for both cases, Figures 10 and 11 present the time evolution of shear-induced bubble deformation and breakup with $Re = 42$ and $Re = 43$, respectively. We note that the bubble critical Reynolds number is around $Re_c \approx 43$, whereas $Re_c \approx 0$ for the corresponding case of the drop with $\lambda = \eta = 1$ (see e.g. Li et al. [24]). Note that Re_c for $Ca = 0.8$ is smaller than that for the condition of $Ca = 0.3$ since the bubble at $Ca = 0.8$ is more elastic due to the weaker effect of surface tension in this case. The results shown in Figs. 10 and 11 indicate that the bubble deformation and breakup process for the condition of $Ca = 0.8$ is analogous to that for $Ca = 0.3$. For the case of bubble deformation without breakup (Fig. 10), the bubble initially assumes a long elongated shape along the x -direction at around $T = 17.0$. The bubble then enters a compression stage over the time interval $[31.3, 41.2]$ and subsequently starts to elongate again at $T = 45.8$. On the other hand, for the case of bubble breakup (Fig. 11), an initial elongation phase is followed by a doglegged shape formation at $T = 33.7$. After that, the bubble ruptures from the thread-bridge part of the doglegged shape and two daughter bubbles are produced ($T = 35.8$). The two daughter bubbles formed after breakup move to the central area ($T = 49.7$) as in the case of $Ca = 0.8$ and $Re = 93$, but the two bubbles eventually coalesce in a region approximately centered in the computational domain ($T = 55.6$). We note that in a real experimental setting, bubbles may coalesce after breaking up due to slight deviations of flow conditions and states. Although the process of bubble deformation and breakup for flow conditions with $Ca = 0.3$ and $Ca = 0.8$ are similar, a pronounced difference is that the bubble for $Ca = 0.8$ is more elongated and slender than that for $Ca = 0.3$ due to the smaller effect of surface

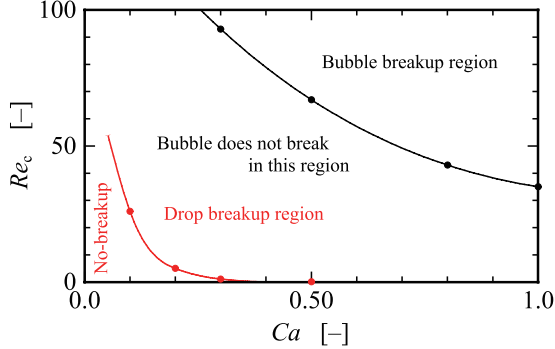


Figure 12: A plot of the critical Reynolds number versus capillary number for the data listed in Table 4. $\lambda = 1.2 \times 10^{-3}$, $\eta < 1.0 \times 10^{-3}$, $0.3 < Ca < 1$, and the initial/boundary conditions are given by (1). Given a new data point, (Ca, Re) , one can reliably predict whether the given (Ca, Re) pair will result in shear induced bubble break-up or not. Note, for the “Drop delineation curve,” $\lambda = \eta = 1$.

615 tension for $Ca = 0.8$.

616 Table 4 lists, for representative Ca values, the corresponding critical Reynolds
 617 number, Re_c , for shear-induced bubble breakup. The data in Table 4 corre-
 618 sponds to $\lambda = 1.2 \times 10^{-3}$, $\eta < 1.0 \times 10^{-3}$, $0.3 < Ca < 1$, and the initial/boundary
 619 conditions are given by (1). The results in Table 4 indicate that sufficiently large
 620 shear forces are required for bubble breakup even for large capillary numbers.
 621 In Figure 12 we plot the smooth interpolant of the data given in Table 4 and
 622 make the hypothesis that given a new data point, (Ca, Re) , shear induced bub-
 623 ble break up will occur if the point (Ca, Re) is above the given critical curve,
 624 and the bubble will not break if the (Ca, Re) pair is below the critical curve.
 625 For comparison, a critical curve for the drop with $\lambda = \eta = 1$ is also indicated
 626 in Fig. 12. The inclusion of breakup and no-breakup critical curves, for both
 627 the drop and the bubble, will facilitate future identification of Re_c numbers—
 628 and thus a more complete general critical curve—for a wide range of high Ca
 629 numbers.

Table 4: Shear-induced bubble breakup for various flow conditions described in terms of column pairs of critical Reynolds numbers and corresponding capillary numbers. ($\lambda = 1.2 \times 10^{-3}$, $\eta < 1.0 \times 10^{-3}$)

	Capillary number Ca	0.3	0.5	0.8	1.0
Critical Reynolds number Re_c		93	67	43	35

630 5. Conclusions

631 The bubble deformation and breakup process in simple linear shear flow
 632 liquid was explored numerically using the CLSVOF computational method. In

633 this study, the critical Reynolds number Re_c , at which bubble breakup first
634 occurs, was determined for several flow conditions, and the differences between
635 bubble deformation and breakup were compared with the well-known analogous
636 process of drop deformation and breakup.

637 Numerical results revealed significant differences between bubble deformation
638 and breakup and the corresponding drop dynamics. For case of bubble,
639 it was discovered that much stronger shear flows are necessary to induce in-
640 terface breakup compared with a drop immersed in a similar flow field. That
641 is, a much larger Reynolds number flow is required in order to induce bubble
642 breakup. The behavior of bubble breakup was very similar through the Ca
643 number range considered in our computations: the bubble underwent a simi-
644 lar breakup mechanism in which rupture occurred at a thread-bridge part that
645 followed a doglegged shape formation stage. In bubble deformation without
646 breakup, near Re_c , the bubble did not maintain a stable deformed shape, in
647 contrast to drop deformation near the critical Reynolds number. The bubble
648 exhibited pronounced underdamped behavior: the bubble oscillated between
649 elongating and shrinking motions for non-rupturing flow conditions. **At the**
650 **same time, bubble deformation under smaller Re conditions ($< Re_c$) becomes**
651 **in a stable state.** We attribute the large differences in morphology for the
652 bubble undergoing breakup, compared with the drop, to the density and viscos-
653 ity ratio. The density and viscosity ratio remarkably impacts on bubble/drop
654 deformation and breakup. The bubble deformation and breakup is subject to a
655 synergistic coupling of the density and viscosity ratio, and whose effect will be
656 examined separately in future work.

657 **References**

- 658 [1] Amani, A., Balcázar, N., Castro, J., Oliva, A., 2019. Numerical study of droplet deformation in shear flow using a con-
659 servative level-set method. *Chemical Engineering Science* 207,
660 153–171. URL: <http://www.sciencedirect.com/science/article/pii/S0009250919305123>, doi:<https://doi.org/10.1016/j.ces.2019.06.014>.
- 664 [2] Bazhlekov, I.B., Anderson, P.D., Meijer, H.E., 2006. Numerical investi-
665 gation of the effect of insoluble surfactants on drop deformation and
666 breakup in simple shear flow. *Journal of Colloid and Interface Sci-
667 ence* 298, 369 – 394. URL: <http://www.sciencedirect.com/science/article/pii/S0021979705012658>, doi:<http://dx.doi.org/10.1016/j.jcis.2005.12.017>.
- 670 [3] Bento, D., Rodrigues, R.O., Faustino, V., Pinho, D., Fernandes, C.S.,
671 Pereira, A.I., Garcia, V., Miranda, J.M., Lima, R., 2018. Deforma-
672 tion of red blood cells, air bubbles, and droplets in microfluidic devices:
673 Flow visualizations and measurements. *Micromachines* 9, 151. URL:
674 <https://www.mdpi.com/2072-666X/9/4/151>, doi:10.3390/mi9040151.

- 675 [4] Chu, P., Finch, J., Bournival, G., Ata, S., Hamlett, C., Pugh, R.J.,
676 2019. A review of bubble break-up. *Advances in Colloid and Interface
677 Science* 270, 108–122. URL: <https://www.sciencedirect.com/science/article/pii/S0001868619300211>, doi:<https://doi.org/10.1016/j.cis.2019.05.010>.
- 680 [5] Cristini, V., Bławzdziewicz, J., Loewenberg, M., 2001. An adaptive
681 mesh algorithm for evolving surfaces: simulations of drop breakup
682 and coalescence. *Journal of Computational Physics* 168, 445 –
683 463. URL: <http://www.sciencedirect.com/science/article/pii/S0021999101967130>, doi:<http://dx.doi.org/10.1006/jcph.2001.6713>.
- 685 [6] Cristini, V., Guido, S., Alfani, A., Bławzdziewicz, J., Loewenberg, M.,
686 2003. Drop breakup and fragment size distribution in shear flow. *Journal
687 of Rheology* 47, 1283–1298. URL: <http://scitation.aip.org/content/sor/journal/jor2/47/5/10.1122/1.1603240>, doi:<http://dx.doi.org/10.1122/1.1603240>.
- 690 [7] Croce, R., Griebel, M., Schweitzer, M.A., 2010. Numerical simulation of
691 bubble and droplet deformation by a level set approach with surface tension
692 in three dimensions. *International Journal for Numerical Methods in Fluids*
693 62, 963–993. URL: <http://dx.doi.org/10.1002/fld.2051>, doi:<10.1002/fld.2051>.
- 695 [8] Drenckhan, W., Saint-Jalmes, A., 2015. The science of foaming. *Advances
696 in Colloid and Interface Science* 222, 228–259. URL: <https://www.sciencedirect.com/science/article/pii/S0001868615000603>,
697 doi:<https://doi.org/10.1016/j.cis.2015.04.001>. Reinhard Miller,
698 Honorary Issue.
- 700 [9] Eftekhari, M., Schwarzenberger, K., Heitkam, S., Eckert, K.,
701 2021a. Interfacial flow of a surfactant-laden interface under asymmetric
702 shear flow. *Journal of Colloid and Interface Science* 599,
703 837–848. URL: <https://www.sciencedirect.com/science/article/pii/S0021979721006457>, doi:<https://doi.org/10.1016/j.jcis.2021.04.126>.
- 706 [10] Eftekhari, M., Schwarzenberger, K., Heitkam, S., Javadi, A.,
707 Bashkatov, A., Ata, S., Eckert, K., 2021b. Interfacial behavior
708 of particle-laden bubbles under asymmetric shear flow. *Langmuir* 37,
709 13244–13254. URL: <https://doi.org/10.1021/acs.langmuir.1c01814>,
710 arXiv:<https://doi.org/10.1021/acs.langmuir.1c01814>. pMID:
711 34726918.
- 713 [11] Ervin, E., Tryggvason, G., 1997. The rise of bubbles in a vertical shear
714 flow. *Journal of Fluids Engineering* 119(2), 443–449.

- 715 [12] Hernandez, F.H., Rangel, R.H., 2017. Breakup of drops in simple
 716 shear flows with high-confinement geometry. Computers & Fluids 146,
 717 23 – 41. URL: <http://www.sciencedirect.com/science/article/pii/S0045793017300038>, doi:<https://doi.org/10.1016/j.compfluid.2017.01.001>.
- 720 [13] Hirt, C., Nichols, B., 1981. Volume of fluid (vof) method
 721 for the dynamics of free boundaries. Journal of Computational
 722 Physics 39, 201 – 225. URL: <http://www.sciencedirect.com/science/article/pii/0021999181901455>, doi:[http://dx.doi.org/10.1016/0021-9991\(81\)90145-5](http://dx.doi.org/10.1016/0021-9991(81)90145-5).
- 725 [14] Inamuro, T., 2006. Lattice boltzmann methods for viscous fluid flows and
 726 for two-phase fluid flows. Fluid Dynamics Research 38, 641. URL: <http://stacks.iop.org/1873-7005/38/i=9/a=A04>.
- 728 [15] Inamuro, T., Tomita, R., Ogino, F., 2003. Lattice boltzmann simulations
 729 of drop deformation and breakup in simple shear flows. International
 730 Journal of Modern Physics B 17, 21–26. URL: <http://www.worldscientific.com/doi/abs/10.1142/S0217979203017035>, doi:10.
 731 1142/S0217979203017035.
- 733 [16] Ioannou, N., Liu, H., Zhang, Y., 2016. Droplet dynamics
 734 in confinement. Journal of Computational Science 17, 463 –
 735 474. URL: <http://www.sciencedirect.com/science/article/pii/S1877750316300308>, doi:<https://doi.org/10.1016/j.jocs.2016.03.009>. discrete Simulation of Fluid Dynamics 2015.
- 738 [17] Janssen, P., Anderson, P., 2008. A boundary-integral model for
 739 drop deformation between two parallel plates with non-unit viscosity
 740 ratio drops. Journal of Computational Physics 227, 8807–
 741 8819. URL: <http://www.sciencedirect.com/science/article/pii/S002199910800346X>, doi:<http://dx.doi.org/10.1016/j.jcp.2008.06.027>.
- 744 [18] Janssen, P.J.A., Anderson, P.D., 2007. Boundary-integral method
 745 for drop deformation between parallel plates. Physics of Fluids
 746 19. URL: <http://scitation.aip.org/content/aip/journal/pof2/19/4/10.1063/1.2715621>, doi:<http://dx.doi.org/10.1063/1.2715621>.
- 748 [19] Kang, M., Fedkiw, R.P., Liu, X.D., 2000. A boundary condition capturing
 749 method for multiphase incompressible flow. Journal of scientific computing
 750 15, 323–360.
- 751 [20] Khismatullin, D.B., Renardy, Y., Cristini, V., 2003. Inertia-induced
 752 breakup of highly viscous drops subjected to simple shear. Physics of Fluids
 753 15, 1351–1354. doi:<http://dx.doi.org/10.1063/1.1564825>.

- 754 [21] Komrakova, A., Shardt, O., Eskin, D., Derksen, J., 2014. Lattice
 755 boltzmann simulations of drop deformation and breakup in shear flow.
 756 International Journal of Multiphase Flow 59, 24 – 43. URL: <http://www.sciencedirect.com/science/article/pii/S0301932213001547>,
 757 doi:<http://dx.doi.org/10.1016/j.ijmultiphaseflow.2013.10.009>.
- 759 [22] Komrakova, A., Shardt, O., Eskin, D., Derksen, J., 2015. Effects
 760 of dispersed phase viscosity on drop deformation and breakup
 761 in inertial shear flow. Chemical Engineering Science 126, 150 –
 762 159. URL: <http://www.sciencedirect.com/science/article/pii/S000925091400726X>, doi:<http://dx.doi.org/10.1016/j.ces.2014.12.012>.
- 765 [23] Legendre, D., Magnaudet, J., 1998. The lift force on a spherical bubble in
 766 a viscous linear shear flow. Journal of Fluid Mechanics 368, 81–126.
- 767 [24] Li, J., Renardy, Y., Renardy, M., 2000. Numerical simulation of
 768 breakup of a viscous drop in simple shear flow through a volume-of-fluid
 769 method. Physics of Fluids 12, 269–282. URL: <http://scitation.aip.org/content/aip/journal/pof2/12/2/10.1063/1.870305>, doi:<http://dx.doi.org/10.1063/1.870305>.
- 772 [25] Müller-Fischer, N., Tobler, P., Dressler, M., Fischer, P., Windhab, E.J.,
 773 2008. Single bubble deformation and breakup in simple shear flow. Experiments
 774 in fluids 45, 917–926.
- 775 [26] Ohta, M., Akama, Y., Yoshida, Y., Sussman, M., 2014. Influence of the
 776 viscosity ratio on drop dynamics and breakup for a drop rising in an im-
 777 miscible low-viscosity liquid. Journal of Fluid Mechanics 752, 383–409.
 778 doi:[10.1017/jfm.2014.339](https://doi.org/10.1017/jfm.2014.339).
- 779 [27] Ohta, M., Furukawa, T., Yoshida, Y., Sussman, M., 2019. A
 780 three-dimensional numerical study on the dynamics and deformation
 781 of a bubble rising in a hybrid carreau and fene-cr modeled poly-
 782 mERIC liquid. Journal of Non-Newtonian Fluid Mechanics 265, 66–
 783 78. URL: <https://www.sciencedirect.com/science/article/pii/S0377025718301952>, doi:<https://doi.org/10.1016/j.jnnfm.2018.12.012>.
- 786 [28] Ohta, M., Kikuchi, D., Yoshida, Y., Sussman, M., 2011. Robust numeri-
 787 cal analysis of the dynamic bubble formation process in a viscous liquid.
 788 International Journal of Multiphase Flow 37, 1059–1071.
- 789 [29] Ohta, M., Sussman, M., 2012. The buoyancy-driven mo-
 790 tion of a single skirted bubble or drop rising through
 791 a viscous liquid. Physics of Fluids 24, 112101. URL:
 792 <https://doi.org/10.1063/1.4765669>, doi:[10.1063/1.4765669](https://doi.org/10.1063/1.4765669),
 793 arXiv:https://pubs.aip.org/aip/pof/article-pdf/doi/10.1063/1.4765669/14128560/112101_1.pdf

- 794 [30] Rallison, J.M., 1984. The deformation of small viscous drops
795 and bubbles in shear flows. Annual Review of Fluid Mechanics
796 16, 45–66. URL: <http://dx.doi.org/10.1146/annurev.fl.16.010184.000401>,
797 doi:10.1146/annurev.fl.16.010184.000401,
798 arXiv:<http://dx.doi.org/10.1146/annurev.fl.16.010184.000401>.
- 799 [31] Renardy, Y., 2006. Numerical simulation of a drop undergoing large am-
800 plitude oscillatory shear. Rheologica acta 45, 223–227.
- 801 [32] Renardy, Y., 2007. The effects of confinement and inertia on the production
802 of droplets. Rheologica Acta 46, 521–529. URL: <http://dx.doi.org/10.1007/s00397-006-0150-y>,
803 doi:10.1007/s00397-006-0150-y.
- 804 [33] Renardy, Y., 2008. Effect of startup conditions on drop breakup under
805 shear with inertia. International Journal of Multiphase Flow
806 34, 1185 – 1189. URL: <http://www.sciencedirect.com/science/article/pii/S030193220800089X>,
807 doi:<http://dx.doi.org/10.1016/j.ijmultiphaseflow.2008.04.004>.
- 809 [34] Renardy, Y., Cristini, V., 2001a. Effect of inertia on drop breakup under
810 shear. Physics of Fluids 13, 7–13. URL: <http://scitation.aip.org/content/aip/journal/pof2/13/1/10.1063/1.1331321>,
811 doi:<http://dx.doi.org/10.1063/1.1331321>.
- 813 [35] Renardy, Y., Cristini, V., Li, J., 2002. Drop fragment distributions un-
814 der shear with inertia. International Journal of Multiphase Flow 28, 1125
815 – 1147. URL: <http://www.sciencedirect.com/science/article/pii/S0301932202000228>,
816 doi:[http://dx.doi.org/10.1016/S0301-9322\(02\)00022-8](http://dx.doi.org/10.1016/S0301-9322(02)00022-8).
- 818 [36] Renardy, Y.Y., Cristini, V., 2001b. Scalings for fragments produced
819 from drop breakup in shear flow with inertia. Physics of Fluids 13,
820 2161–2164. URL: <https://doi.org/10.1063/1.1384469>,
821 doi:10.1063/1.1384469, arXiv:<https://doi.org/10.1063/1.1384469>.
- 822 [37] Rust, A., Manga, M., 2002. Bubble shapes and orientations in low re-
823 simple shear flow. Journal of Colloid and Interface Science 249, 476–
824 480. URL: <https://www.sciencedirect.com/science/article/pii/S0021979702982925>,
825 doi:<https://doi.org/10.1006/jcis.2002.8292>.
- 826 [38] Sharifi, R., Varmazyar, M., Mohammadi, A., 2024. Investigat-
827 ing droplet and bubble deformation under shear flow us-
828 ing the multi-pseudo-potential scheme of lattice boltzmann
829 method. Advances in Applied Mathematics and Mechanics
830 16, 519–548. URL: <https://global-sci.com/article/72820/investigating-droplet-and-bubble-deformation-under-shear-flow-using-the-multi-pseudo-potential-scheme-of-lattice-boltzmann-method>,
831 doi:<https://doi.org/10.4208/aamm.OA-2021-0326>.

- 833 [39] Stone, H.A., 1994. Dynamics of drop deformation and breakup
 834 in viscous fluids. Annual Review of Fluid Mechanics 26,
 835 65–102. URL: <http://dx.doi.org/10.1146/annurev.fl.26.010194.000433>,
 836 doi:10.1146/annurev.fl.26.010194.000433, arXiv:<http://dx.doi.org/10.1146/annurev.fl.26.010194.000433>.
- 838 [40] Sussman, M., 2003. A second order coupled level set and volume-
 839 of-fluid method for computing growth and collapse of vapor bubbles.
 840 Journal of Computational Physics 187, 110–136. URL: <https://www.sciencedirect.com/science/article/pii/S0021999103000871>,
 841 doi:[https://doi.org/10.1016/S0021-9991\(03\)00087-1](https://doi.org/10.1016/S0021-9991(03)00087-1).
- 843 [41] Sussman, M., Almgren, A.S., Bell, J.B., Colella, P., Howell, L.H.,
 844 Welcome, M.L., 1999. An adaptive level set approach for incom-
 845 pressible two-phase flows. Journal of Computational Physics 148, 81
 846 – 124. URL: <http://www.sciencedirect.com/science/article/pii/S002199919896106X>, doi:<https://doi.org/10.1006/jcph.1998.6106>.
- 848 [42] Sussman, M., Puckett, E.G., 2000. A coupled level set and
 849 volume-of-fluid method for computing 3d and axisymmetric incompress-
 850ible two-phase flows. Journal of Computational Physics 162, 301–
 851 337. URL: <http://www.sciencedirect.com/science/article/pii/S0021999100965379>, doi:<http://dx.doi.org/10.1006/jcph.2000.6537>.
- 853 [43] Sussman, M., Smereka, P., Osher, S., 1994. A level set ap-
 854 proach for computing solutions to incompressible two-phase flow.
 855 Journal of Computational Physics 114, 146 – 159. URL: <http://www.sciencedirect.com/science/article/pii/S0021999184711557>,
 856 doi:<http://dx.doi.org/10.1006/jcph.1994.1155>.
- 858 [44] Sussman, M., Smith, K., Hussaini, M., Ohta, M., Zhi-Wei, R., 2007. A
 859 sharp interface method for incompressible two-phase flows. Journal of Com-
 860 putational Physics 221, 469–505. URL: <https://www.sciencedirect.com/science/article/pii/S0021999106002981>, doi:<https://doi.org/10.1016/j.jcp.2006.06.020>.
- 863 [45] Tanguy, S., Ménard, T., Berlemont, A., 2007. A level set method for
 864 vaporizing two-phase flows. Journal of Computational Physics 221, 837–
 865 853.
- 866 [46] Tatebe, O., 1993. The multigrid preconditioned conjugate gradient method,
 867 in: NASA. Langley Research Center, The Sixth Copper Mountain Confer-
 868 ence on Multigrid Methods, Part 2.
- 869 [47] Taylor, G.I., 1932. The viscosity of a fluid containing small drops of another
 870 fluid. Proceedings of the Royal Society of London A: Mathematical, Phys-
 871 ical and Engineering Sciences 138, 41–48. doi:10.1098/rspa.1932.0169.

- 872 [48] Taylor, G.I., 1934. The formation of emulsions in definable fields of flow.
873 Proceedings of the Royal Society of London A: Mathematical, Physical and
874 Engineering Sciences 146, 501–523. doi:10.1098/rspa.1934.0169.
- 875 [49] Unverdi, S.O., Tryggvason, G., 1992. A front-tracking method
876 for viscous, incompressible, multi-fluid flows. Journal of Computational
877 Physics 100, 25 – 37. URL: <http://www.sciencedirect.com/science/article/pii/002199919290307K>, doi:[http://dx.doi.org/10.1016/0021-9991\(92\)90307-K](http://dx.doi.org/10.1016/0021-9991(92)90307-K).
- 880 [50] Wang, A., Evans, G., Mitra, S., 2023. A review of bubble surface loading and its effect on bubble dynamics. Minerals Engineering 199, 108105. URL: <https://www.sciencedirect.com/science/article/pii/S089268752300119X>, doi:<https://doi.org/10.1016/j.mineng.2023.108105>.
- 885 [51] Wang, Z., Shi, D., Zhang, A., 2015. Three-dimensional lattice boltzmann simulation of bubble behavior in a flap-induced shear flow. Computers & Fluids 123, 44 – 53. URL: <http://www.sciencedirect.com/science/article/pii/S0045793015003199>, doi:<https://doi.org/10.1016/j.compfluid.2015.09.007>.
- 890 [52] Wei, Y.K., Qian, Y., Xu, H., 2012. Lattice boltzmann simulations of single bubble deformation and breakup in a shear flow. The Journal of Computational Multiphase Flows 4, 111–117. URL: <https://doi.org/10.1260/1757-482X.4.1.111>, doi:10.1260/1757-482X.4.1.111, arXiv:<https://doi.org/10.1260/1757-482X.4.1.111>.
- 895 [53] Yoshikawa, H.N., Zoueshtiagh, F., Caps, H., Kurowski, P., Petitjeans, P., 2010. Bubble splitting in oscillatory flows on ground and in reduced gravity. The European Physical Journal E 31, 191–199.
- 898 [54] Zhang, J., Miksis, M.J., Bankoff, S.G., 2006. Nonlinear dynamics of a two-dimensional viscous drop under shear flow. Physics of Fluids 18. URL: <http://scitation.aip.org/content/aip/journal/pof2/18/7/10.1063/1.2222336>, doi:<http://dx.doi.org/10.1063/1.2222336>.
- 902 [55] Zhang, J., Ni, M.J., Magnaudet, J., 2021a. Three-dimensional dynamics of a pair of deformable bubbles rising initially in line. part 1. moderately inertial regimes. Journal of Fluid Mechanics 920, A16.
- 905 [56] Zhang, J., Ni, M.J., Magnaudet, J., 2022. Three-dimensional dynamics of a pair of deformable bubbles rising initially in line. part 2. highly inertial regimes. Journal of Fluid Mechanics 943, A10.
- 908 [57] Zhang, J., Shu, S., Guan, X., Yang, N., 2021b. Regime mapping of multiple breakup of droplets in shear flow by phase-field lattice boltzmann simulation. Chemical Engineering Science 240, 116673. URL: <https://www.sciencedirect.com/science/article/>

912 pii/S0009250921002384, doi:<https://doi.org/10.1016/j.ces.2021.116673>.

914 [58] Zhang, W., Almgren, A., Beckner, V., Bell, J., Blaschke, J., Chan, C.,
915 Day, M., Friesen, B., Gott, K., Graves, D., Katz, M., Myers, A., Nguyen,
916 T., Nonaka, A., Rosso, M., Williams, S., Zingale, M., 2019. AMReX: a
917 framework for block-structured adaptive mesh refinement. Journal of Open
918 Source Software 4, 1370. URL: <https://doi.org/10.21105/joss.01370>,
919 doi:10.21105/joss.01370.